UVIT Imaging of WLM: Demographics of Star-forming Regions in the Nearby Dwarf Irregular Galaxy

Chayan Mondal , Annapurni Subramaniam, and Koshy George
Indian Institute of Astrophysics, Koramangala II Block, Bangalore-560034, India; chayan@iiap.res.in, mondalchayan1991@gmail.com
Received 2018 May 17; revised 2018 July 4; accepted 2018 July 18; published 2018 August 21

Abstract

We present a study of star-forming regions and their demographics in the nearby dwarf irregular galaxy WLM using Ultraviolet Imaging Telescope (UVIT) multiband observations in three filters, F148W, N245M, and N263M. We find that the UV emission is extended at least up to 1.7 kpc, with the NUV emission more extended than the FUV. We create UV color maps ((F148W − N245M) and (F148W − N263M)) to study the temperature morphology of young stellar complexes with the help of theoretical models. We identify several complexes with temperature $T > 17,500$ K, which are likely to be OB associations present in the galaxy. These complexes show good spatial correlation with the Hα-emitting regions, H I distribution, and *HST*-detected hot stars. The hot star-forming regions are found to be clumpy in nature and show a hierarchical structure, with sizes in the range of 4–50 pc, with a large number with sizes <10 pc. The southwestern part of the galaxy shows many hot star-forming regions, high levels of Hα emission, and low column density of H I, which altogether denote vigorous recent star formation. WLM is likely to have a large fraction of low-mass compact star-forming regions with mass $M < 10^3 M_\odot$, in agreement with the size and mass of the CO clouds. We estimate the star formation rate of WLM to be ~0.008 $M_\odot$ yr^{-1}, which is similar to the average value measured for nearby dwarf irregular galaxies.

Key words: galaxies: dwarf – galaxies: individual – galaxies: star formation – Local Group

1. Introduction

Dwarf galaxies are the most abundant type of galaxy in the universe. These are the building blocks of galaxy formation and evolution, and they formed when the universe was very young. In the hierarchical merging LCDM paradigm, the stellar halos of the massive galaxies in the local universe are thought to have accumulated from the continuous merging of dwarf galaxies. Despite their number and proximity, however, they are still among the least understood objects. Understanding the factors that allow these dwarf galaxies to survive to the present day may explain the discrepancies between the observed and predicted distribution of such galaxies in and around the Milky Way. This requires an understanding of how internal and environmental effects are expected to shape the evolution of low-mass systems like dwarf galaxies. These galaxies have low metallicity and a shallow potential well, and hence understanding how star formation proceeds in such regimes is crucial in the study of their counterparts in the early universe (Weisz et al. 2011; Bianchi et al. 2012). While massive galaxies formed most of their stars in the first few gigayears, dwarf galaxies have been found to form stars over the entire cosmic time, resulting in a wide variety of star formation histories (Tolstoy et al. 2009; McQuinn et al. 2015; Cignoni et al. 2018) and specific star formation rates, ranging from nearly inactive dwarfs to very active blue compact dwarfs (BCDs).

Nearby dwarf galaxies offer a unique opportunity to study star formation in a low-mass and metal-poor environment. Leaman et al. (2012) presented a detailed discussion of the possible mechanisms that keep star formation alive in dwarf galaxies, despite their shallow potential well. The absence of a spiral density wave makes them an ideal laboratory to understand the effect of internal triggering mechanisms, such as feedback from massive stars (Hunter 1997). These internal triggers mainly have a localized effect in the interstellar medium of the galaxy. In order to understand these internal triggers, it is important to identify the distribution of hot massive stars in the galaxy. As the young and hot stars are easily detected in the ultraviolet (UV), the extent and structure of the UV disk for any dwarf galaxy are excellent probes to study the global star-forming activities in the galaxy (Hunter et al. 2010).

WLM is a faint dwarf irregular galaxy of the Local group, located at a distance of 995 kpc (Urbaneja et al. 2008). It was first discovered by Wolf (1909) and later confirmed by Melotte (1926), thus the reason it is named WLM (Wolf–Lundmark–Melotte; Dolphin 2000). The nearest neighbor of WLM, located 175 kpc away, is the small dSph galaxy Cetus (Whiting et al. 1999), whereas the massive spirals MW, M31, and M33 are about 1 Mpc away (Minniti & Zijlstra 1997). Due to its isolated location in the sky, it is believed that the galaxy has not interacted with other galaxies since its creation. This is demonstrated in Figure 1 of Leaman et al. (2012). A study of Leo A, an isolated dwarf irregular galaxy, by Cole et al. (2007) showed that the star formation pattern and chemical evolution can be different in isolated dwarfs from those present in a galaxy group (Weisz et al. 2011). The metal-poor environment (log $Z = −0.87$; Urbaneja et al. 2008) of WLM has made it an ideal laboratory for studying such isolated systems. The parameters of WLM are presented in Table 1.

Young massive OB stellar populations are found to have intense UV continuum flux due to their high temperature. Imaging studies in UV broadbands can identify the young and massive groups of stars, whereas optical bands get contributions from low-mass stars. The UV images of nearby star-forming galaxies from the *GALEX* mission made a phenomenal contribution in the last decade (Gil de Paz et al. 2007; Thilker et al. 2007; Karachentsev & Kaisina 2013). The Ultraviolet Imaging Telescope (UVIT; Kumar et al. 2012) on *ASTROSAT*, with its superior spatial resolution, is expected to provide better

Table 1
Properties of WLM

Property	Value	References
R.A.	00:01:57.8	Gallouet et al. (1975)
Decl.	−15:27:51.0	Gallouet et al. (1975)
Morphological type	IB(s)m	de Vaucouleurs (1991)
Distance	995 ± 46 kpc	Urbaneja et al. (2008)
Metallicity (log $(Z/Z_\odot)$)	−0.87 ± 0.06	Urbaneja et al. (2008)
Inclination	69°	de Vaucouleurs (1991)
PA of major axis	181°	de Vaucouleurs (1991)

insight into the physics of star formation in galaxies (George et al. 2018a, 2018b, 2018c). Here, we present the details of star formation in the WLM galaxy, based on UVIT observations in one FUV broadband and two NUV medium-band filters.

Previous photometric studies found this galaxy to have a relatively metal-rich younger disk with an old metal-poor halo (Ferraro et al. 1989; Minniti & Zijlstra 1997; Dolphin 2000; Rejkuba et al. 2000). Melena et al. (2009) studied the UV-bright regions in 11 dwarf irregular galaxies including WLM. They detected 165 bright UV regions in the galaxy WLM using *GALEX* data and estimated their age and mass, assuming them to be star clusters. The cluster formation was found to have a constant rate, which stopped 22 Myr ago. They found the UV disk to be more extended than the Hα disk of the galaxy. A recent *HST* study by Bianchi et al. (2012) covered the galaxy in three *HST* pointings and detected a rich population of young and hot stars in the 1–10 Myr age range.

The H I disk of the galaxy is also well studied and found to be more extended than either the optical or UV disk. Kepley et al. (2007) used VLA observation to map the H I density distribution of the galaxy and found a hook-like structure near the center. They concluded that the star formation propagating out from the center of the galaxy created this pattern. Using ALMA observations, Rubio et al. (2015) identified several CO cloud cores in the galaxy. The presence of these low-mass clouds provided new insight into such a metal-poor environment and revealed the possibility of low-mass cluster formation in the galaxy.

In this study, we examined the FUV and NUV emission profile of WLM with the help of UVIT multiband observations. We make use of the broadband FUV filter, F148W, which is similar to the *GALEX* FUV filter, to map the FUV emission. We use two medium-band NUV filters, N245M and N263M, to study the NUV emission. These filters, along with the FUV filter, are used to make the UV color maps. One of the filters, N245M is located in the wing of the 217.5 nm extinction feature whereas N263M is unaffected, and therefore is used to address the issue of dust extinction. Here we use the FUV − NUV color to derive the temperature of the hot SF regions and estimate their temperature distribution with the help of theoretical models. This study thus provides the demographics of massive OB stars in WLM. The paper is arranged as follows. The data are presented in Section 2, models are discussed in Section 3, the effect of extinction and metallicity in Section 4, analysis in Section 5, followed by a discussion and summary in Sections 6 and 7, respectively.

2. Data

The UV images of WLM were obtained from UVIT on board the *ASTROSAT* satellite (Kumar et al. 2012). The instrument consists of two co-aligned telescopes, each having an aperture of 375 mm. One of the telescopes observes in the FUV band (1300–1800 Å), while the other one observes in both NUV (2000–3000 Å) and the visible. The telescopes are capable of observing simultaneously in the FUV, NUV, and visible bands. The visible channel is used to correct the drift pattern in the UV imaging data introduced by the satellite during the course of the observation. Each of the FUV, NUV, and visible channels consists of multiple filters having different bandwidths, which indeed is unique, particularly for the UV passbands. The telescope has a 28 arcmin circular field of view with an angular resolution of ∼1.5 arcsec. It can resolve sources much better than *GALEX* (4.5–5.5 arcsec). The in-orbit calibration of the instrument is completed using HZ4 as a calibration source. We refer to Tandon et al. (2017) for all of the calibration measurements adopted in this paper. The observations for the galaxy WLM were taken in three filters, one in the FUV band (F148W: 1250–1750 Å) and two in the NUV bands (N245M: 2148–2710 Å and N263M: 2461–2845 Å). The complete observation was carried out using multiple orbits of the *ASTROSAT* satellite with a 90 minute period on an equatorial orbit. Data for each of the orbit were corrected for spacecraft drift using the specialized software CCDLAB (Postma & Leahy 2017). We also corrected the data for fixed pattern noise and spatial distortion, which are intrinsic to the detector (Postma et al. 2011; Girish et al. 2017). All of the images of the respective filters are then flat-fielded, co-aligned, and combined to produce deeper images, which are shown in Figure 1. The final exposure time obtained for the filters F148W, N245M, and N263M as well as the filter characteristics are tabulated in Table 2. The UVIT images have slightly less than twice the *GALEX* exposure times of WLM (Melena et al. 2009). All images have 4096 × 4096 pixel dimension, with 1 pixel corresponding to 0.4125 arcsec, which is equivalent to ∼2 pc at the distance of WLM. Since there are not enough FUV-bright field stars available in the UVIT field of view (Figure 1), we used the model point spread function (PSF) image for the F148W filter created for the galactic globular cluster NGC 1851 (Subramaniam et al. 2017). In the case of the two NUV filters, the model PSFs were built from the field stars present in the UVIT field. The FWHM of the model PSF for both the F148W and N263M filters, which are primarily used in our analysis, is 1″.5. The image in the N245M filter, which is mainly used for comparison, has a PSF of 1″.7.

We have also used the Hα image of the galaxy observed with the CTIO 4.0 m telescope (Massey et al. 2007) and the neutral hydrogen (H I) map from the VLA telescope (Kepley et al. 2007) in our study. Both images were obtained from the NASA Extragalactic Database (NED).

3. Theoretical Models

As we plan to identify hot star-forming regions based on the UV colors, we need to establish a relation between the UV colors (i.e., the flux ratio between UVIT filters) and temperatures. We used Castelli & Kurucz (2004) stellar models, which offer a stellar spectrum for different temperatures between 3500–50,000 K, to derive the above relation. For a fixed temperature, individual spectra are available for different surface gravities (log g) and metallicities (log Z). We fixed the metallicity as log $Z = -0.5$ (which is close to that of WLM; Urbaneja et al. 2008, Table 1) and surface gravity log $g = 5.0$ and selected 13 spectra in the temperature range 3500–50,000 K. The spectra are then convolved with the effective area profile of the UVIT filters to calculate the expected flux (Tandon et al. 2017).
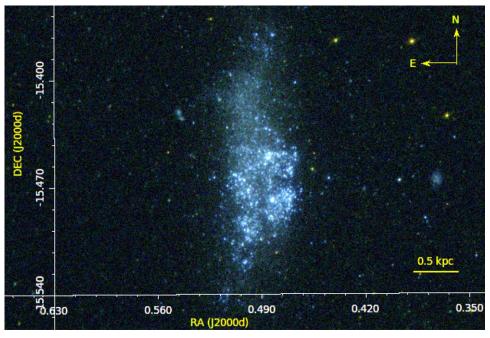
Figure 1. False-color composite image of the galaxy WLM. The galaxy is observed in three different UVIT filters, F148W, N245M, and N263M, which are represented by the blue, green, and red colors respectively.

Table 2
Details of UVIT Observations

Filter	Bandpass (Å)	ZP Magnitude (AB)	Unit Conversion (erg/s/cm²/Å)	$\triangle\lambda$ (Å)	Exposure Time (s)
F148W	1250–1750	18.016 ± **0.01**	3.09×10^{-15}	500	2634
N245M	2148–2710	18.50 ± **0.07**	7.25×10^{-16}	280	1926
N263M	2461–2845	18.18 ± **0.01**	8.44×10^{-16}	275	2370

We created diagnostic plots as shown in Figure 2 (blue curve) by taking the ratio of fluxes for two different combinations of filters (i.e., $\mathrm{Flux_{F148W}}/\mathrm{Flux_{N263M}}$ in Figure 2(a) and $\mathrm{Flux_{F148W}}/\mathrm{Flux_{N245M}}$ in Figure 2(b)). The other curves in the same plots are generated after including the effect of extinction according to different extinction laws, which is discussed in the next section. These curves are used to estimate the temperature distribution as well as to identify the potential locations of OB associations.

We further used the Starburst99 simple stellar population (SSP) model (Leitherer et al. 1999) to generate the diagnostic diagrams shown in Figure 3 to characterize the identified compact star-forming regions. Starburst99 is a spectrophoto-metric SSP model for actively star-forming galaxies. We obtained Starburst99 model data for the parameters listed in Table 3. We assumed the star formation to be instantaneous for the estimations. The IMF value is taken to be 1.3 (for 0.1 $M_{\odot}$ to 0.5 $M_{\odot}$) and 2.3 (for 0.5 $M_{\odot}$ to 120 $M_{\odot}$, Kroupa IMF; Kroupa 2001), with stellar mass limits of $M_{\mathrm{low}} = 0.1\,M_{\odot}$ and $M_{\mathrm{up}} = 120\,M_{\odot}$, which are appropriate for studying SSPs up to a few 100 Myr. We produced model grids for the F148W magnitude as a function of (F148W − N263M) color. In order to convert the model-generated fluxes into magnitude values, we adopted a distance of 995 kpc (Urbaneja et al. 2008) for WLM. We considered four different values for the total cluster mass ($10^6\,M_{\odot}$, $10^5\,M_{\odot}$, $10^4\,M_{\odot}$, $10^3\,M_{\odot}$) and a fixed metallicity of $Z = 0.004$ to generate Figure 3. The dashed

lines are generated by adding the extinction and reddening to each of the actual model curves (continuous lines) shown for the different masses. The points shown in each curve signify different ages from 1 to 900 Myr (increasing along the color axis). From Figure 3, we find that, for a fixed age (equivalently color), massive clusters are brighter.

4. Effect of Extinction and Metallicity

The behavior of the extinction curve in the UV region shows a noticeable variation for different external galaxies. It is observed that the extinction coefficient in FUV and NUV changes from galaxy to galaxy or even within a galaxy. The 2175 Å bump is an important feature of the Galactic extinction curve, and it also shows a characteristic variation for external galaxies. Gordon et al. (2003) reported the differential nature of the extinction curve in the UV for the LMC, SMC, and Milky Way galaxies. Therefore, it is important for us to first understand the nature of the extinction law that applies to the star-forming regions of WLM, and second, to understand how the fluxes in the UVIT filters are affected by the extinction law. In Figure 4, we show the behavior of the different extinction laws such as the Fitzpatrick law (for the Milky Way; Fitzpatrick 1999), Calzetti law (for starburst regions; Calzetti et al. 1994), and the average LMC, LMC 30 Dor, and SMC bar (Gordon et al. 2003), along with the UVIT filter profiles. The
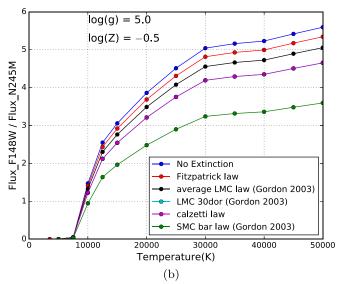
(a)

(b)

Figure 2. The relation between the UV flux ratio and temperature, estimated using Kurucz spectra, for log g = 5.0 and log Z = −0.5. The F148W/N263M and F148W/N245M flux ratios are shown in panels (a) and (b), respectively. The blue curves in both panels are without extinction correction. The other curves are generated by applying an extinction on the blue curve from the different extinction laws mentioned in the figure.

Figure 3. Starburst99 model-generated color–magnitude plots for a simple stellar population. The figure shows the F148W magnitude with (F148W − N263M) color. The different curves (continuous lines) signify four different total cluster masses ($10^6 M_\odot$, $10^5 M_\odot$, $10^4 M_\odot$, $10^3 M_\odot$). The dashed lines show the extinction- and reddening-corrected values for each model curve. The points shown in each curve are for different ages starting from 1 Myr to 900 Myr (increasing along the color axis) with age interval 10 Myr for the 1 to 100 Myr range and 100 Myr for 100 to 900 Myr. The values of the other parameters adopted for this figure are listed in Table 3.

Table 3
Starburst99 Model Parameters

Parameter	Value
Star formation	Instantaneous
Stellar IMF	Kroupa (1.3, 2.3)
Stellar mass limit	0.1, 0.5, 120 $M_\odot$
Total cluster mass	$10^3 M_\odot$–$10^6 M_\odot$
Stellar evolution track	Geneva (high mass loss)
Metallicity	$Z = 0.004$
Age range	1–900 Myr

data for the extinction curves are obtained from the extinction calculator (McCall 2004) available on the NED website. It is quite clear that the N245M filter profile partially overlaps with the 2175 Å bump of the extinction curve. Assuming the average value of R_λ within the bandpass of each filter and adopting $E(B − V) = 0.082$ (Gieren et al. 2008), we estimated the extinction value (A_λ) for different extinction laws using the general transformation law given in Equation (1). The extinction-corrected flux ratios after incorporating different extinction laws are shown in Figure 2. Since the behavior of extinction in UV in extragalactic studies is highly debated, the simulated plots in Figure 2 highlights the possible uncertainty in the estimated temperature for a fixed flux ratio.

In their study of the properties of *HST*-identified stars, Bianchi et al. (2012) concluded that the most suitable extinction law for the star-forming regions of WLM is the average LMC type (Gordon et al. 2003). In our study, we
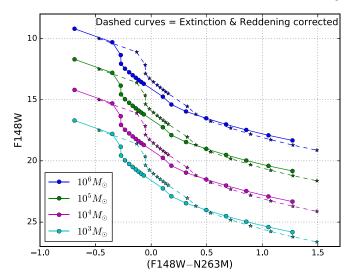
adopted the UV extinction of WLM to be the average LMC type and calculated the value of R_λ and A_λ for all three UVIT filters, which are given in Table 4.

Considering the possibility of a spread in the metallicity across the star-forming regions, we explored the effect of metallicity in the estimated temperature. It turns out that as log Z changes from −0.5 to −1.0, the corresponding change in the flux ratio for the different temperatures is found to be negligible (Figure 5). The metallicity of WLM, measured from a spectroscopic study of blue supergiants present in the galaxy, is reported to be −0.87 by Urbaneja et al. (2008). As the effect of metallicity is not very sensitive to the derived temperature, we consider log $Z = −0.5$ for the Kurucz model spectra.

$$A_\lambda = R_\lambda E(B − V). \qquad (1)$$

5. Analysis

5.1. Extent of UV Emission

We consider the F148W band image to study the extent of UV emission in WLM, which in turn traces the expanse of hot and young massive stars. The FUV-emitting regions as shown in Figure 1 are found to be highly structured. Many regions could be massive complexes comprising a large number of
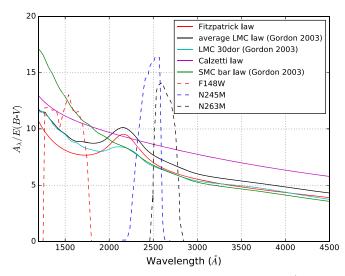
Figure 4. The variation of the extinction coefficient (R_λ, i.e., $A_\lambda/E(B-V)$) with wavelength for different extinction laws. The solid lines of different colors represent the different laws mentioned in the figure. The scaled effective area curves for the three UVIT filters are also shown by the dashed lines.
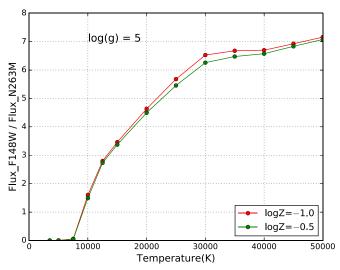

Figure 5. The flux ratio $Flux_{F148W}/Flux_{N263M}$ is plotted with temperature for two different metallicities, $\log Z = -1.0$ and -0.5.

Table 4
Extinction Parameters for the Average LMC Law (Gordon et al. 2003)

Filter	R_λ	A_λ
F148W	9.78	0.80
N245M	8.40	0.69
N263M	7.07	0.58

smaller groups, which are not resolved in our images, while some are found to be much smaller, suggestive of smaller groups and, in a few cases, individual associations of OB stars. In order to locate the brightest and hence massive complexes, we created a low-resolution map of size 512×512, where each pixel corresponds to 3.3 arcsec, which is equivalent to ~16 pc at the distance of WLM. Each pixel value of the image denotes the integrated count of a stellar group having size ~16×16 pc^2. As we target the locations of large complexes and their sizes, we created contours by fixing the lower and upper limits of the flux values, which are given in Table 5
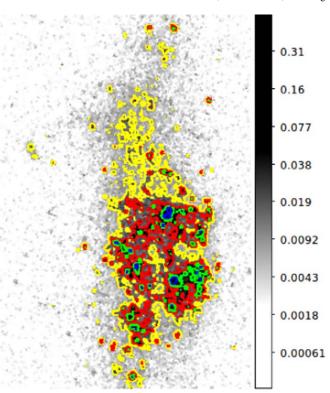

Figure 6. The background figure is the 512×512 F148W band image of WLM with contours plotted for different limits of the F148W flux values as mentioned in Table 5. The blue contours represent the brightest (hence most massive) regions of the galaxy. The overall extent of the FUV emission of WLM is traced by the yellow contours.

Table 5
Details of the Flux and Magnitudes for the Contours in the F148W Map Shown in Figure 6

$\log(Flux_{F148W})$ Range [erg/s/cm^2/Å]	Magnitude Range (Extinction Uncorrected)	Contour Color
>-15.3	<20	Blue
-15.7 to -15.3	>20 and <21	Green
-16.1 to -15.7	>21 and <22	Red
-16.5 to -16.1	>22 and <23	Yellow

(shown in Figure 6). The blue contours show pixels brighter than 20 magnitude. These are the most luminous star-forming complexes present in the galaxy. We find that at this FUV magnitude, the contributing compact star-forming regions are likely to be more massive than $10^3 M_\odot$ (see Figure 3). The counts per second (CPS) corresponding to this FUV magnitude is 0.16, and there are only a few regions that have a CPS greater than this value (see Figure 6). We are able to identify three luminous (extended) regions, which are shown in blue. The green and red contours, which signify relatively less bright regions, are found to be present around these regions, suggestive of a hierarchical structure. The yellow contours generated for pixels fainter than 22 mag and brighter than 23 mag portray the overall extent of the FUV emission.

We further studied the structure of emission in two NUV images (N245M and N263M). Using similar 512×512 images, we generated contours for pixels brighter than 23 mag for both NUV images. For comparison, the blue, green, and red contours
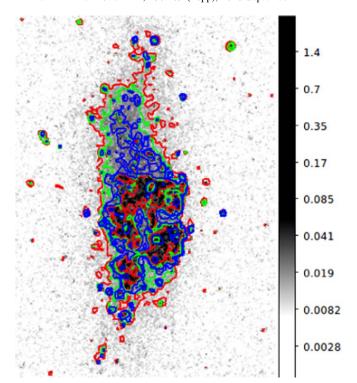
Figure 7. The background figure is the 512 × 512 N263M band image of WLM. The blue, green, and red contours shown in the figure are generated for pixels brighter than 23 mag in the F148W, N245M, and N263M filter images, respectively. The FUV emission (blue contours) is seen to be enveloped by both green and red contours representing the NUV emission of WLM.

Figure 8. The background figure is the 512 × 512 N263M band image of WLM. The blue, green, and red contours shown in the figure are generated for pixels brighter than 23.80, 23.69, and 23.58 mag (adding the effect of extinction), respectively, in the F148W, N245M, and N263M filter images. The extent of the NUV emission as traced in the N263M filter is found to be greater than that of Figure 7.

generated for images in the F148W, N245M and N263M bands, respectively, are overlaid on the N263M image (Figure 7). It is clearly seen that the extent of UV emission gradually increases as we go toward longer wavelengths. The red contours, signifying the emission in the NUV N263M filter, are found to be stretched more outwardly than the green (N245M) and blue (F148W) contours. The FUV emission, traced by the blue contours, is found to be present inside the extent of both NUV emissions (green and red contours). As the contours shown above are likely to be affected by extinction, we apply the extinction correction and reproduce the contours. Applying the average LMC law for extinction (Gordon et al. 2003), the extinction-corrected magnitudes are 23.80, 23.69, and 23.58 mag for the F148W, N245M, and N263M filters, respectively. The blue, green, and red contours shown in Figure 8 are generated for the above magnitudes in the F148W, N245M, and N263M filter images, respectively. Again, the morphology of the FUV and NUV emission is found to be similar to Figure 7. The NUV emission as traced by the N263M filter is found to be more extended in Figure 8 than in Figure 7. As the FUV traces a hotter and more massive population, when compared to the NUV, it is clear that these are located in the inner part of the galaxy, whereas relatively cooler, less massive stellar populations are present in the outer regions.

5.2. Luminosity Density Profile

The radial variation of the luminosity density in UV conveys the characteristic distribution of star-forming regions in any active galaxy. Since WLM is observed in one FUV and two NUV filters of UVIT, we constructed the radial surface
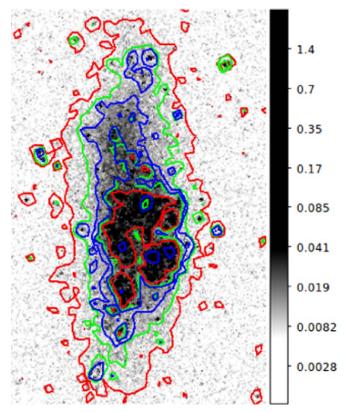
luminosity density profile in all filters. Assuming the inclination and position angle of the galaxy (Table 1), we estimated the galactocentric distance to each pixel in all three images, using the relation given in van der Marel & Cioni (2001). Starting from the galaxy center (R.A. and decl. given in Table 1), we considered annuli of width 0.1 kpc and measured the total CPS in each individual annuli, up to a radius of 2 kpc. The total CPS value is then corrected for background and extinction. The average background in CPS/kpc^2 in all three images is calculated by considering three similar annuli of width 0.1 kpc from radii of 2.5 kpc to 2.8 kpc. The luminosities in each annuli are then estimated by assuming the distance to WLM to be 995 kpc, and considering the respective values of the unit conversion factor and bandwidth of each filter from Table 2. The surface luminosity density ($erg\,s^{-1}\,pc^{-2}$) as a function of radius is shown in Figure 9. The luminosity density in all three filters shows a dip in the central part of the galaxy and peaks at around 0.4 kpc (in F148W it is ∼0.5 kpc) from the center, which signifies that the star formation is relatively less active near the center of WLM. Beyond 0.4 kpc, it decreases again toward the outer part of the galaxy. In order to investigate the relative flux variation between the far- and near-UV, we further plotted the (F148W – N245M) and (F148W – N263M) radial color profile in Figure 10. From the center to 0.5 kpc, both colors become bluer with radius. After 0.5 kpc, the trend changes and the colors start becoming redder with respect to the value at 0.5 kpc. Beyond 1 kpc, the colors become redder than the average value in the inner 1 kpc. Again, the (F148W – N263M) color is found to be bluer than the (F148W – N245M)
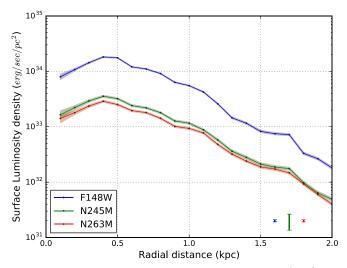
Figure 9. The profile for the surface luminosity density (erg s^{-1} pc^{-2}) with galactocentric distance in kiloparsecs for three UVIT filters. The UV emission of WLM is found to be extended at least up to a radius of 1.7 kpc. The shaded region corresponding to each curve shows the 5σ photometric error whereas the error bars (bottom right) represents the 5σ error due to the present uncertainty of the adopted zero-point magnitudes.
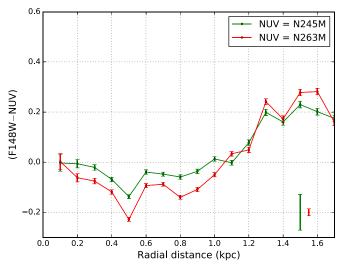

Figure 10. The variation of the (F148W − N245M) and (F148W − N263M) colors is shown versus galactocentric distance in kiloparsecs. Both profiles remain nearly flat in the inner 1 kpc whereas an upturn is noticed for the outer part beyond 1 kpc. The photometric errors are shown in the profile, and the error bars displayed in the bottom-right corner signify the error due to the uncertainty in zero-point magnitudes.

color in the inner 1 kpc region, whereas it becomes almost similar outside 1 kpc. This fact can be interpreted as the outer part beyond 1 kpc having a relatively large extinction and/or a lower number of massive stars when compared to the inner part.

5.3. UV Color Maps

We use the FUV and NUV images to create the UV color maps to trace the temperature profiles of star-forming regions. All three images are first co-aligned and normalized with respect to their exposure time. The image in the F148W filter is divided by the images in the N263M and N245M filters to create the F148W/N263M and F148W/N245M images, respectively. The pixel value of each of these resultant images

Table 6
Details of the Flux Ratio and Temperature for the (F148W − N263M) Color Map, as Shown in Figure 11

(Flux$_{F148W}$/Flux$_{N263M}$) Range	Temperature Range (K)	Contour Color
>5.23	>35,000	Blue
4.43 to 5.23	>25,000 and <35,000	Red
3.18 to 4.43	>17,500 and <25,000	Green

is actually the CPS ratio in the respective filters. We infer the temperature corresponding to each pixel of the F148W/ N263M (or F148W/N245M) image with the help of Figure 2. We consider the black curve, which is generated according to the average LMC-type extinction law (Gordon et al. 2003), of both Figures 2(a) and (b).

5.4. (F148W − N263M) Color Map

We first considered the (F148W − N263M) color map to investigate the temperature profiles of the star-forming regions. Considering the black curve of Figure 2(a), we fixed the upper and lower limits of the flux ratio to different values to create different contour sets signifying the different temperature ranges, which are listed in Table 6. We adopted a smoothness of 2 pixels (∼4 pc), which helps to trace smaller regions as well. We divided the galaxy into five different regions and designated them as R1, R2, R3, R4, and R5. Their locations are shown in Figure 11(a). We adopt the same temperature used by Bianchi et al. (2012) to classify the regions. The blue contours signify regions with very high temperatures ($T > 35,000$ K, corresponding to early O-type stars), while the red contour indicates intermediate-temperature regions ($25,000$ K $< T < 35,000$ K, late O-type stars), and the green contours indicate relatively low-temperature ($17,500$ K $< T < 25,000$ K, early B-type stars) regions (Table 6). Regions that are not covered by any of these three contours suggest temperatures less than 17,500 K. Regions R1 to R5, with overlaid contours, are shown in Figures 11(b) to (f). Thus, the regions covered by these contours are occupied by OB stars. The high-temperature regions (blue contour) are found to be enveloped by relatively lower temperature regions (red and green contours) throughout the galaxy. These show the hierarchical structure of actively star-forming regions.

The southwestern part (R1) is found to have several high-temperature regions (blue contour) of different sizes. Though the regions have irregular shape, an approximate size can be assigned by measuring their longest dimension. The largest high-temperature complex identified in R1 is L-shaped, with a north–south extent of ∼50 pc, and an east–west extent of ∼40 pc. The width of the region is in the range of ∼20–30 pc. This is the largest massive complex in WLM. We also found nearly 10 regions of size >20 pc. The smaller regions (<10 pc) are more scattered and large in number, with the smallest of them with sizes ∼4 pc. The red contours signifying intermediate temperature are found to connect several hot regions (blue contour) and form knotted structures. There are also more smaller (∼4 pc), low-temperature regions than similar-sized, hotter regions. The nature of the temperature gradient around each hot star-forming region (blue contour) is clearly depicted by the red and green contours present around them.

The region R2 is assigned to the southern part of the galaxy. We identify three high-temperature regions of size ∼30 pc and a large number of smaller regions with sizes <10 pc. One clumpy hot region is identified at the extreme south of the
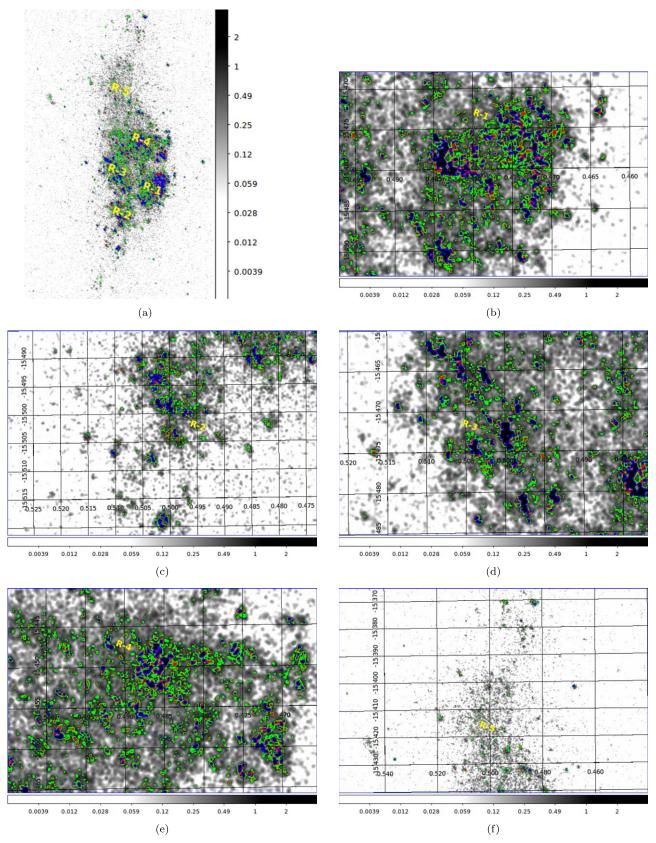
(a)

(b)

(c)

(d)

(e)

(f)

Figure 11. The (F148W − N263M) color map of the galaxy is shown with different plotted contours. Panel (a) shows the whole galaxy along with the specified positions of five regions, R1, R2, R3, R4, and R5. The blue, red, and green contours are generated for different flux limits, signifying different temperature ranges as mentioned in Table 6. The background image shown here is smoothed, and the grayscale denotes the logarithmic value of the CPS ratio for the smoothed image. We have shown zoomed-in images for regions R1, R2, R3, R4, and R5 in panels (b), (c), (d), (e), and (f), respectively. The regions marked by the blue contours denote the hotter regions of the galaxy.

Table 7
Details of the Flux Ratio and Temperature for the (F148W − N245M) Color
Map, as shown in Figure 12

(Flux$_{F148W}$/Flux$_{N245M}$) Range	Temperature Range (K)	Contour Color
>4.64	>35,000	Blue
4.09 to 4.64	>25,000 and <35,000	Red
3.15 to 4.09	>17,500 and <25,000	Green

galaxy, which appears to be almost detached from the main body of the galaxy. The eastern part of the galaxy (R3) is found to have a greater number of larger-sized high-temperature regions, with eight complexes of size larger than 20 pc and one region extending up to ∼50 pc in length. These eight complexes are spatially isolated from each other and distributed along the southwest to northeast direction. Around some of these large complexes, we noticed smaller (<10 pc) hot regions, which are connected by the red contours. The scenario for the R4 (north and northwestern part) region is a little different. Though the region has a larger spatial extent than the rest, we do not detect any large structure with very high temperature, but rather an abundance of structures scattered all around it. We also identify two locations (one along the north and another along the west) with an increased number of scattered structures. The extreme northern part of the galaxy (R5) does not show any high-temperature region except for two or three isolated hot star-forming clumps.

Therefore, the star-forming regions of WLM are found to have an overall hierarchical structure with the hottest cores surrounded by relatively less hotter regions. It is also clear that the young star-forming regions are fragmented and clumpy in nature.

5.5. (F148W − N245M) Color Map

In order to explore the effect of differential extinction inside the galaxy and to study the detected hot star-forming regions further, we performed the same exercises for the color map (F148W − N245M) (i.e., the F148W/N245M image). The model-generated diagram for tracing the temperature in the (F148W − N245M) color map is shown in Figure 2(b) (blue curve). The UV color image with the overlaid contours is shown in Figure 12(a), and the temperatures corresponding to the different contours are given in Table 7. The expanded view of the R1, R2, R3, R4, and R5 regions is shown in Figures 12(b) to (f). It is natural to expect the shape and distribution of the identified hot star-forming regions to be similar in nature in both color maps. We notice that, although the overall distribution of hot star-forming regions in both color maps match each other in general, a closer look reveals a more fragmented structure in the (F148W − N245M) color map. The larger complexes detected in the (F148W − N263M) color maps split into smaller regions in the (F148W − N245M) color map. This could happen because of two reasons. The differential behavior of the 2175 Å bump inside the galaxy can change the effective extinction value, which affects the observed flux value in the N245M filter. This in turn can produce the structural differences of the star-forming regions between the two color maps. The same effect can also be produced by a clumpy distribution of hot stars, which have more flux in the N245M filter. Thus, we conclude that either the young and hot stellar groups, or the dust present in WLM, or both, have a clumpy distribution.

5.6. Correlating with Hα and H I Maps

We correlate the spatial distribution of the UV-detected high-temperature regions in the color map (i.e., (F148W − N263M)) with the Hα and H I images of the galaxy. Since Hα radiation mainly comes from gas ionized by massive and hot OB-type stars, it is expected that the UV-detected high-temperature regions will show a good spatial correlation with Hα-emitting regions. In Figure 13, along with the contours (blue and red) created in the (F148W − N263M) color map, we have shown the Hα-emitting regions of the galaxy in cyan contours. Almost all of the high-temperature regions detected in R1, R2, R3, and R4 appear inside the cyan contours, which indeed signifies a good spatial correlation between them. In the R1 region, we notice a hole in the Hα map which does not have any detected UV hot region near its center, though we detect a few smaller hot regions within the hole. We identify a large number of hot regions located to the north of the hole, with a reduced number of such regions in the southern side. We identify several clumpy and knotted hot regions west of the R1 region with much less Hα emission. In R2, there are two major hot clumps that also show Hα. All of the hot regions detected in the R3 region correlate well with Hα-emitting regions. The shapes of the Hα contours also match with the overall distribution pattern of high-temperature regions. In the R4 region, the detected clumps of hot regions are enveloped by Hα emission. The elongation of the central Hα contour in R4 along the west and south is also traced well by the hot regions. The overall good spatial correlation between Hα-emitting regions and UV-detected hot complexes confirms the presence of massive O- and early B-type stars in these complexes.

Further, we spatially correlate these hot star-forming regions with the neutral hydrogen (H I) density map of the galaxy. Since stars are mainly formed from molecular clouds, the presence of hydrogen gas would support the possibility of recent star formation. Kepley et al. (2007) identified a hook-like overdensity pattern in the H I distribution as shown in Figure 14. The hook-shaped magenta contour is found to cover almost all of the high-temperature regions except those in R1. Therefore, the R1 region is found to have many UV-detected hot star-forming clumps showing Hα emission (except for some parts in the west—Figure 13), but with a relatively low H I density. This may be the result of a vigorous recent star formation in R1, where the H I gas is ionized/driven away after star formation. Other hot regions in R2, R3, and R4 are found to have a high column density of H I along with Hα emission.

5.7. Correlating with HST-detected Hot Stars

Bianchi et al. (2012) observed the galaxy WLM with six *HST* broadband filters (F170W, F255W, F336W, F439W, F555W, F814W) and noticed a richness of stars with age younger than 10 Myr. The bluest band used in their observation is F170W with a bandwidth of 1200–2400 Å. Stars that are bright in the F170W band are expected to be hot, young, and relatively massive. We spatially correlated the hot regions detected in our study with stars that are brighter than 19 mag in the F170W band from their photometric catalog. Excluding some part of R3, the regions R1, R2, R3, and R4 are almost fully covered by the three *HST* fields observed in their study. In Figure 15, we have overlaid these stars on top of the (F148W − N263M) color map. The detected stars (cyan box) show a good spatial correlation with the hot star-forming regions (blue and
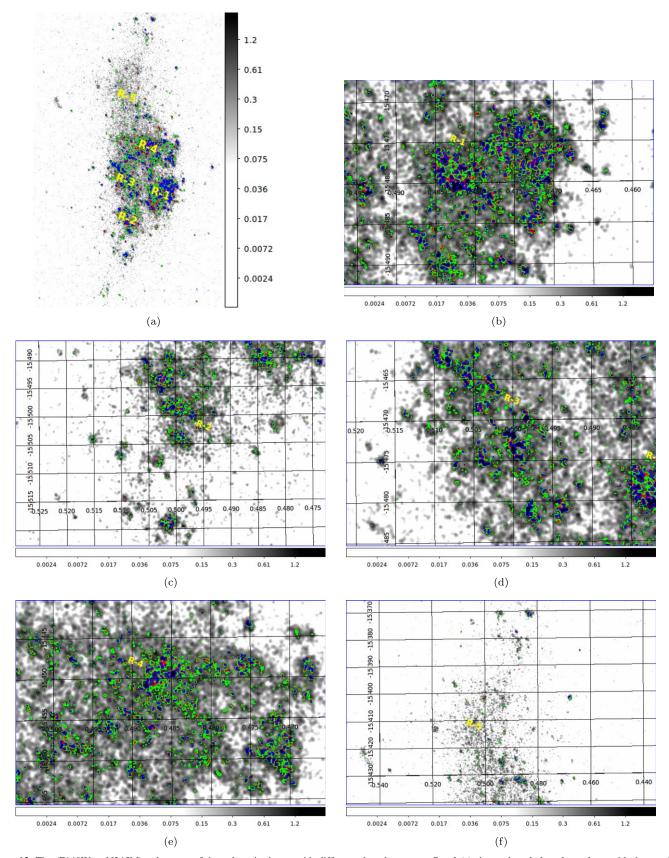
Figure 12. The (F148W − N245M) color map of the galaxy is shown with different plotted contours. Panel (a) shows the whole galaxy along with the specified position of five regions, R1, R2, R3, R4, and R5. The blue, red, and green contours are generated for different flux limits signifying different temperature ranges as mentioned in Table 7. The background image shown here is smoothed, and the grayscale denotes the logarithmic value of the CPS ratio for the smoothed image. We have shown zoomed-in images for regions R1, R2, R3, R4, and R5 in panels (b), (c), (d), (e), and (f), respectively. The regions marked by the blue contours are found to be more fragmented than those in Figure 11.

Figure 13. Hα image of the galaxy WLM, covering regions R1, R2, R3, and R4, is shown in the background where the grayscale signifies the logarithmic value of CPS. The cyan contours signify the Hα-emitting regions of the galaxy. The plotted blue and red contours are the same as shown in Figure 11(a). The UV-detected hot regions show a good spatial correlation with the Hα-emitting regions of the galaxy.
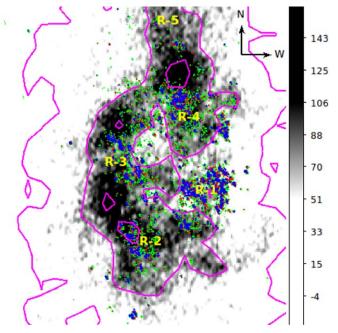

Figure 14. The background image shows the H I density distribution of the galaxy WLM. The hook-like magenta contour is the overdensity pattern reported by Kepley et al. (2007). The plotted blue, red, and green contours are the same as those shown in Figure 11(a). R1 has several UV-detected hot-forming regions with lower H I density. Other regions (R2, R3, R4, and R5) are found to have dense H I gas.

red contours) of the galaxy. This confirms that massive young stars are co-located with the high-temperature star-forming regions identified in our study.

5.8. Mass Estimation of Compact Star-forming Regions

In the UVIT images, some of the star-forming regions were found to appear like point sources, due to their small sizes. As there are a good number of them, many of these are likely to be part of WLM, though a small fraction could belong to the

background. We assumed all of the detected point sources to be the compact star-forming regions of the galaxy and performed PSF photometry to estimate their magnitudes. In order to estimate mass, we considered the filters F148W and N263M for which we have simulated the model diagram in Figure 3. After cross-matching the individually detected star-forming regions in the F148W and N263M filters, we identified 590 common regions. In Figure 16, we plotted the observed star-forming regions (gray points) along with the model curves as previously shown in Figure 3 to estimate the mass of these regions. Most of the detected star-forming regions have colors within the model range, whereas we do detect a significant number of sources with bluer colors. These may be due to background sources, and hence we consider only those that appear within the model limit. The majority of the compact star-forming regions are found to have mass $M < 10^3 M_\odot$ with some of them between $10^3 M_\odot$ and $10^4 M_\odot$. A few regions are found to have $M > 10^5 M_\odot$, but could be older as indicated by their color. Therefore, the galaxy WLM is found to have a large number of young low-mass compact star-forming regions with $M < 10^3 M_\odot$.

5.9. Correlating with CO Observations

Since molecular clouds are the sites of star formation, we correlate our results with recent CO observations of WLM. With the help of ALMA, Rubio et al. (2015) observed two 1 arcmin² field in WLM with a spatial resolution of 6.2 pc × 4.3 pc, which is comparable with UVIT. They identified 10 CO clouds with an average radius of 2 pc and an average virial mass of $2 \times 10^3 M_\odot$. In Figure 17, we have shown the positions of detected CO clouds (green circles) in the two targeted fields (northwest (NW) and southeast (SE)), shown with black square boxes. The same blue and red contours in Figure 11 are also shown to correlate the position of the detected molecular clouds with the hot star-forming regions. In Figure 18, we zoom in to these regions where CO clouds are detected (black box in Figure 17). Along with the spatial position, we show the size and virial mass of each cloud as estimated by Rubio et al. (2015). The majority of the detected clouds are of low mass (∼$10^3 M_\odot$), which in principle supports our finding of a large number of low-mass compact star-forming regions in WLM. Again, the absence of higher mass molecular clouds could be the reason for the absence of massive compact star-forming regions in this galaxy. We further find that eight of the detected CO clouds are found to be present away from the hot star-forming regions. The only two clouds that are found to be co-located (there could also be a projection effect) with the hot star-forming regions are NW-1 and SE-4, where SE-4 is the most massive cloud detected.

5.10. Star Formation Rate

In order to estimate the star formation rate (SFR) of WLM, we used the F148W band (FUV) exposure normalized image of the galaxy. We summed up the flux (CPS) within a galactocentric distance of 1.7 kpc, which is the extent of WLM's outer disk as found in Section 5.2. The background-corrected total flux is converted to magnitude and further corrected for extinction. The background- and extinction-corrected magnitude is used to calculate the total SFR of the galaxy ($M_\odot \, yr^{-1}$). The corrected FUV flux is found to be $7.0 \times 10^{-13} \pm 3.6 \times 10^{-15}$ erg/s/cm²/Å and the corresponding magnitude 12.12 ± 0.01. We used the scaling relation,
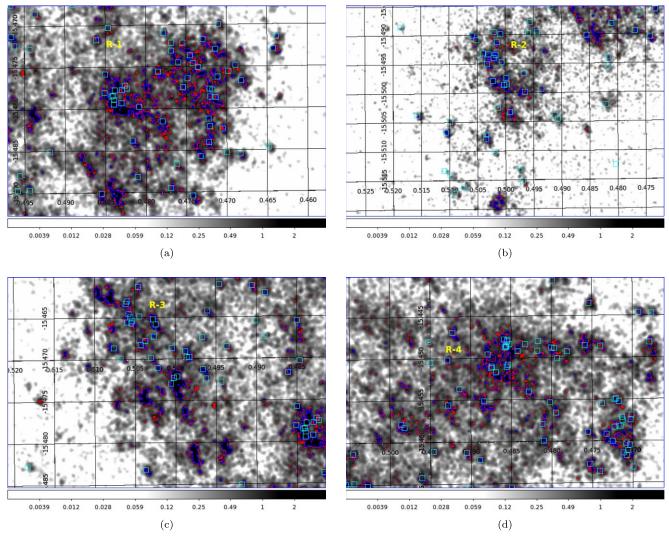
Figure 15. F148W/N263M smoothed image is shown with the same blue and red contours as plotted in Figure 11. The *HST*-detected massive stars (cyan box) are overlaid on regions R1, R2, R3, and R4 as shown in panels (a), (b), (c), and (d), respectively.
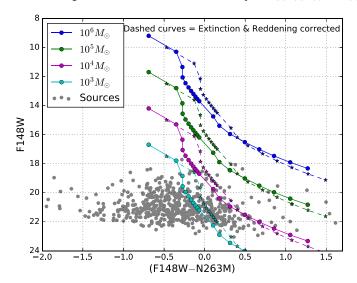

Figure 16. The identified compact star-forming regions are overplotted (gray filled circles) on Starburst99 model curves.

given in Equation (2) (Karachentsev & Kaisina 2013), to estimate the SFR, where mag$_{FUV}$ is the corrected FUV magnitude and D is the distance to the galaxy in Mpc. Karachentsev & Kaisina (2013)

used this relation to estimate the SFR of a large sample of galaxies in the local volume using *GALEX* FUV observations. Since the F148W filter of UVIT has bandpass similar to the *GALEX* FUV, we used this relation to estimate the SFR. The total SFR up to a radial distance of 1.7 kpc is found to be $0.008 \pm 0.0001\, M_\odot\, \mathrm{yr}^{-1}$. This value of SFR could change if we adopt a different scaling relation. For example, if we adopt the empirical relation modeled by McQuinn et al. (2015), we estimate the SFR of WLM to be in the range 0.002–$0.006\, M_\odot\, \mathrm{yr}^{-1}$.

In order to explore the radial variation of the SFR within WLM, we generated the radial profile of the SFR density (i.e., $M_\odot\, \mathrm{yr}^{-1}\, \mathrm{kpc}^{-2}$). The radial variation of the SFR density is shown in Figure 19. The SFR density is found to increase with radius up to 0.4 kpc, resulting in a peak at this radius. The SFR density decreases after 0.4 kpc in the outer part, where the profile is shown up to 2 kpc. The profile also suggests that the SFR density is dominated by regions within a radius of 1 kpc. The relative positions of all the regions (R1, R2, R3, R4) along with the position angle is shown in Figure 20. This figure shows that most of these regions are located within the 1 kpc radius. We further explored the azimuthal variation of the SFR density by taking the radially averaged value up to 2 kpc in Figure 21. The profile shows two peaks at diametrically opposite values of the position
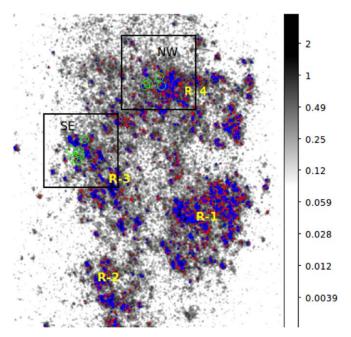
Figure 17. The smoothed F148W/N263M image is shown in the background with the logarithmic grayscale. The blue and red contours signify the hot regions of the galaxy as in Figure 6(a). Two black squares (one in the northwest (NW) and another in the southeast (SE)) are the two 1 arcmin² ALMA fields observed by Rubio et al. (2015) to detect CO clouds. The green circles shown inside the boxes are the positions of detected CO clouds.
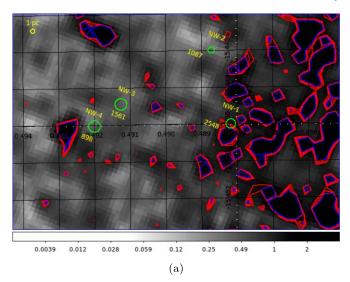

(a)

(b)

Figure 18. Panels (a) and (b) show the zoomed-in view of the regions (inside the two black boxes in Figure 17) where CO detection is found in the northwest (NW) and southeast (SE) fields, respectively. The background image and contours are the same as those mentioned in Figure 17. The CO clouds are shown with green circles, where the size of the circles signifies the size of the cloud with respect to the 1 pc reference circle shown in each figure. The clouds are labelled as per Rubio et al. (2015). The numbers shown near each green circle signify its virial mass in $M_\odot$.

angle ($\sim 0°$ and $180°$). The peak near PA $\sim 0°$ has a contribution from the northern regions R4 and R5, whereas the peak at PA $\sim 180°$ has contributions from R1, R2, and R3. Figures 21 and 20 suggest that the southern half of the galaxy has a slightly higher SFR density when compared to the northern half.

$$\log(\mathrm{SFR_{FUV}}(M_\odot\,\mathrm{yr}^{-1})) = 2.78 - 0.4 * \mathrm{mag_{FUV}} + 2\log(D). \tag{2}$$

6. Discussion

The primary objective of this study is to identify hot star-forming regions of the dwarf irregular galaxy WLM and to map its demographics. We used the UV images of the galaxy acquired from UVIT, which has a superior spatial resolution (~ 1.5 arcsec). The hot star-forming regions are identified from the UV color maps with the help of the temperature–flux ratio relation derived from Kurucz spectra. We point out that this relation may change with any corresponding change in the assumed value of metallicity, extinction, and surface gravity of stars. We demonstrate that the change of metallicity value between 0.002 to 0.006 has a negligible effect on the flux ratio, and hence on the measured temperature. On the other hand, the estimated parameters will have a dependence on the assumed extinction and its variation. Figure 2(a) shows the range of temperature for a given flux ratio, for various extinction laws. It also suggests that the uncertainty in temperature due to extinction is greater for a higher temperature.

For any dwarf galaxy, feedback from massive stars acts as one of the dominant mechanisms for driving star formation. According to the study of Dolphin (2000), WLM formed half of its stars 9 Gyr ago and showed a reduction in star formation rate after that. They also found that the star-forming activity increased around 1 to 2.5 Gyr, which continues until now.
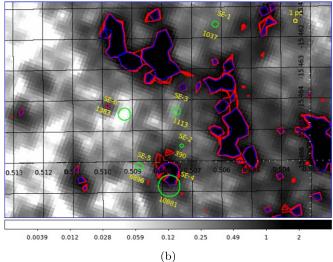
Bianchi et al. (2012) found that the galaxy underwent vigorous star formation during the last 10 Myr. They found 531 stars with temperature $T > 18,000$ K and 721 stars having $M > 9\,M_\odot$. In this study, we detect several hot regions with $T > 35,000$ K, which are likely to be populated by O-type stars. As the lifetimes of these stars are ~ 10 Myr, this would suggest that WLM has undergone recent star formation activity with the production of massive stars. We also notice that the hot regions are surrounded by relatively cooler regions, suggestive of a hierarchical structure. These are in agreement with the findings of Bianchi et al. (2012). We identified around 20 hot complexes with a size of 20–50 pc and more than 50 complexes with a size of 10–20 pc. Regions with size <10 pc are found to be large in number (up to a few hundred) and scattered over a larger area of the galaxy. The smaller regions have lower masses and are likely to be populated by a few OB stars, whereas the larger ones are likely to be complexes consisting of two or more associations of the galaxy.
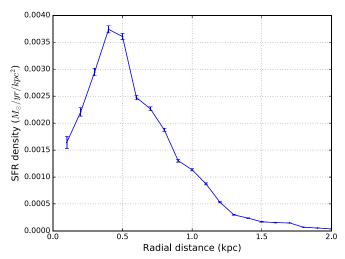
Figure 19. The radial profile for the SFR density ($M_\odot$ yr^{-1} kpc^{-2}) with the 3σ error bar is shown in the figure.
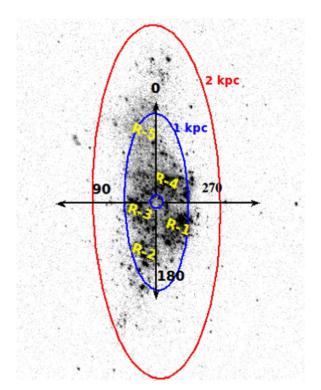

Figure 21. The azimuthal variation of the radially averaged (up to 2 kpc) SFR density ($M_\odot$ yr^{-1} kpc^{-2}) with the 3σ error bar is shown in the figure. Two peaks at PA $\sim 0°$ and $180°$ signify the contribution of star-forming regions from the northern and southern half of the galaxy, respectively.

Figure 20. The figure shows all five regions (R1, R2, R3, R4 and R5) with the F148W band image in the background. The black arrows show the position angle along four different directions. The blue and red ellipses represent 1 kpc and 2 kpc galactocentric distances, respectively.

Our study finds that WLM is dominated by small-sized regions, with the largest complex not exceeding 50 pc.

It is well known that the star formation creates hierarchical structures comprising star clusters, OB associations, and complexes (Efremov & Elmegreen 1998; Bastian et al. 2007; Sun et al. 2018). These structures are found to have various sizes and densities in various environments (Elmegreen et al. 2014; Grasha et al. 2017). Bresolin et al. (1998) studied OB associations in seven nearby spiral galaxies using *HST*-WFPC2 data and found a size range of $\sim$70–100 pc. For nearby irregular galaxies, the size of OB associations is reported to be $\sim$80 pc by Ivanov (1996). Mel'Nik & Efremov (1995) found a relatively smaller size ($\sim$10–80 pc, with a peak around 30 pc) for galactic OB associations, whereas
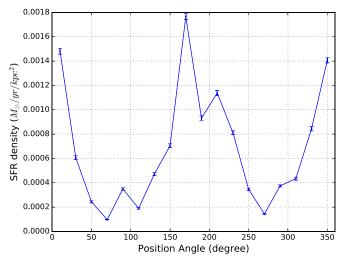
for LMC and SMC, it is around 60 pc (Bresolin et al. 1996). Bastian et al. (2007) noted the star formation in M33 to be hierarchical in nature with a size distribution of young stellar complexes between 10–100 pc. Garcia et al. (2010) studied IC 1613, a similar nearby dwarf irregular galaxy like WLM, and concluded the star formation to be hierarchical with no specific length scale. The OB associations identified in their study show a size of $\sim$14–42 pc, which is quite similar to our findings in WLM. Garcia et al. (2010) also found that 44% of the total associations are smaller in size. Several studies conclude that the size of these detected associations is highly dependent on the resolution of the telescope and the distance to the galaxy (Bastian et al. 2007; Garcia et al. 2010). Due to the better spatial resolution of UVIT, we are able to detect smaller substructures of the star-forming regions present in the galaxy, when compared to *GALEX*. The overall sizes of the OB associations in WLM, detected through UVIT, are found to be quite similar to those in IC 1613 (nearby dwarf irregular), but smaller than those in M33 (nearby spiral) and the Milky Way.

Around most of the larger hot complexes, we detect the presence of several smaller regions connected together by low-temperature contours. This brings out the clumpy nature of the star-forming regions in WLM. The feedback from the massive stars (large hot complexes) may have triggered further star formation in their proximity, which results in these clumpy distribution of young star-forming regions. We also noticed that the relatively low-temperature regions are much more spread out than the hot regions, which is also mentioned in the study by Bianchi et al. (2012). The star-forming regions also show several knotted structures, specifically in R1. The overall distribution of detected hot star-forming regions throughout the galaxy clearly reveals that the southern part of the galaxy is much more active than its northern part. The hot star-forming regions detected in the (F148W − N245M) color map are found to be more fragmented than those seen in the (F148W − N263M) color map. A clumpy distribution of either the young stellar objects or the dust or both of them present in the galaxy can result in these observed structural differences.

We also studied the extent of UV emission in WLM. We noticed that the NUV emission as traced by the N245M and

N263M filters is more extended than the FUV emission. Since the FUV emission mainly comes from the younger stellar populations, it is probable that the populations present in the outer part of the galaxy are relatively older than those in the inner part. The luminosity density profile clearly shows that the UV emission of the galaxy is present at least up to a radius of 1.7 kpc.

A high-resolution H I study by Kepley et al. (2007) revealed the presence of a hook-like structure in the H I distribution. They speculated that an expanding ring-like structure broke in the western part and generated this hook-like pattern. They concluded that this structure is likely to be the result of star formation propagating outside from the center of the galaxy. The hot regions detected in our study delineate this hook structure except in the western part (i.e., in R1). The H I density shows an overall reduction in R1 whereas we see intense Hα emission with a central hole in the same region. On the basis of this scenario, Kepley et al. (2007) concluded that H I is likely to be used up or ionized or destroyed due to the high rate of star formation in this part of the galaxy. In our study, we detected several knotted structures of hot star-forming regions in R1 which signify the presence of several OB stars. This region also has one of the three most luminous star-forming complexes (see Figure 6). This L-shaped complex is located to the north and is suggestive of intense recent star formation. We also notice hot star-forming regions forming an arc-like shape, located to the west of the Hα ring (see Figure 13). This might suggest that the Hα emission is shrinking toward the inner hole, on the eastern side. The western arc-like structure could be relatively older with respect to the northern complex. The radiation from these OB stars has probably driven/consumed the H I gas present there, which supports the scenario of Kepley et al. (2007).

In a recent study with ALMA observations, Rubio et al. (2015) detected several CO clouds with sizes ranging from 3 to 12 pc in diameter. The smaller hot star-forming regions (i.e., clusters or OB associations) identified in our study have an average size from 4 to 20 pc, with most of them with sizes <10 pc. The comparable sizes of the CO clouds and hot star-forming regions suggest that star formation happens in smaller molecular clouds in this galaxy. The masses estimated for the compact star-forming regions detected in this study also match well with the mass of the CO clouds, confirming the formation of low-mass stellar clumps.

We estimated the total FUV magnitude to be 12.12 ± 0.01 mag, corresponding to an SFR of $\sim 0.008 \pm 0.0001\, M_\odot\, \mathrm{yr}^{-1}$. As mentioned earlier, the value of the SFR is a function of the scaling relation and could change if a different relation is used. Earlier estimations by Karachentsev & Kaisina (2013) and Hunter et al. (2010) using *GALEX* FUV observations are comparable. Though the SFR of WLM is lower compared to that of the Milky way ($1.9 \pm 0.4\, M_\odot\, \mathrm{yr}^{-1}$; Chomiuk & Povich 2011), the value of the specific SFR (sSFR = SFR/stellar mass of galaxy) of WLM is 16 times higher than that of the Milky Way. For the total stellar mass of WLM ($1.6 \times 10^7\, M_\odot$; Zhang et al. 2012) and the Milky Way ($(6.4 \pm 0.6) \times 10^{10}\, M_\odot$; McMillan 2011), the estimated values of the sSFR are 5.0×10^{-10} and $3.0 \times 10^{-11}\, \mathrm{yr}^{-1}$, respectively. Therefore, being a dwarf irregular galaxy, WLM is able to form stars at a relatively higher rate than the Milky way (Rubio et al. 2015).

7. Summary

The main results of this study are summarized below:

1. The UVIT images in the FUV and NUV are used to study the demographics of the star-forming regions in WLM.
2. The UV emission of WLM is found to be present up to a galactocentric distance of 1.7 kpc, with most of the flux originating within a radius of 1 kpc.
3. We divided the galaxy into five different regions to compare the demographics and identified the three most luminous and massive star-forming complexes, with the largest one extending not more than 50 pc.
4. The hot star-forming regions with $T > 17{,}500\, \mathrm{K}$ (populated with OB stars) have a range of sizes, with a few tens of regions in the 20–50 pc range and a few hundred regions with <10 pc size.
5. The hot stellar regions are found to be surrounded by regions with cooler stars, suggesting a hierarchical nature of distribution.
6. The presence of several hot regions suggests that the galaxy underwent a recent star formation ~ 10 Myr ago.
7. We find a good spatial correlation between UV-detected hot regions and Hα-emitting regions, H I distribution, and *HST*-detected massive stars in the galaxy. The western part (R1) of the galaxy is likely to have undergone a vigorous recent star formation.
8. The sizes and masses of isolated star-forming regions closely match with those of CO clouds estimated using ALMA observations. WLM is found to have a large number of low-mass ($M < 10^3\, M_\odot$) compact star-forming regions.
9. The star formation in the southern part of the galaxy is more active than the northern part. The SFR of the galaxy is $\sim 0.008\, M_\odot\, \mathrm{yr}^{-1}$, which is similar to that found in other dwarf galaxies.

ORCID iDs

Chayan Mondal https://orcid.org/0000-0003-4531-0945
Koshy George https://orcid.org/0000-0002-1734-8455

References

Bastian, N., Ercolano, B., Gieles, M., et al. 2007, MNRAS, 379, 1302
Bianchi, L., Efremova, B., Hodge, P., Massey, P., & Olsen, K. A. G. 2012, AJ, 143, 74
Bresolin, F., Kennicutt, R. C., Jr., Ferrarese, L., et al. 1998, AJ, 116, 119
Bresolin, F., Kennicutt, R. C., Jr., & Stetson, P. B. 1996, AJ, 112, 1009
Calzetti, D., Kinney, A. L., & Storchi-Bergmann, T. 1994, ApJ, 429, 582
Castelli, F., & Kurucz, R. L. 2004, arXiv:astro-ph/0405087
Chomiuk, L., & Povich, M. S. 2011, AJ, 142, 197

Cignoni, M., Sacchi, E., Aloisi, A., et al. 2018, ApJ, 856, 62
Cole, A. A., Skillman, E. D., Tolstoy, E., et al. 2007, ApJL, 659, L17
de Vaucouleurs, G. 1991, Sci, 254, 1667
Dolphin, A. E. 2000, ApJ, 531, 804
Efremov, Y. N., & Elmegreen, B. G. 1998, MNRAS, 299, 588
Elmegreen, D. M., Elmegreen, B. G., Adamo, A., et al. 2014, ApJL, 787, L15
Ferraro, F. R., Fusi Pecci, F., Tosi, M., & Buonanno, R. 1989, MNRAS, 241, 433
Fitzpatrick, E. L. 1999, PASP, 111, 63
Gallouet, L., Heidmann, N., & Dampierre, F. 1975, A&AS, 19, 1
Garcia, M., Herrero, A., Castro, N., Corral, L., & Rosenberg, A. 2010, A&A, 523, A23
George, K., Joseph, P., Côté, P., et al. 2018a, arXiv:1802.09493
George, K., Joseph, P., Mondal, C., et al. 2018b, arXiv:1805.03543
George, K., Poggianti, B. M., Gullieuszik, M., et al. 2018c, arXiv:1803.06193
Gieren, W., Pietrzyński, G., Szewczyk, O., et al. 2008, ApJ, 683, 611
Gil de Paz, A., Boissier, S., Madore, B. F., et al. 2007, ApJS, 173, 185
Girish, V., Tandon, S. N., Sriram, S., Kumar, A., & Postma, J. 2017, ExA, 43, 59
Gordon, K. D., Clayton, G. C., Misselt, K. A., Landolt, A. U., & Wolff, M. J. 2003, ApJ, 594, 279
Grasha, K., Calzetti, D., Adamo, A., et al. 2017, ApJ, 840, 113
Hunter, D. 1997, PASP, 109, 937
Hunter, D. A., Elmegreen, B. G., & Ludka, B. C. 2010, AJ, 139, 447
Ivanov, G. R. 1996, A&A, 305, 708
Karachentsev, I. D., & Kaisina, E. I. 2013, AJ, 146, 46
Kepley, A. A., Wilcots, E. M., Hunter, D. A., & Nordgren, T. 2007, AJ, 133, 2242
Kroupa, P. 2001, MNRAS, 322, 231

Kumar, A., Ghosh, S. K., Hutchings, J., et al. 2012, Proc. SPIE, 8443, 84431N
Leaman, R., Venn, K. A., Brooks, A. M., et al. 2012, ApJ, 750, 33
Leitherer, C., Schaerer, D., Goldader, J. D., et al. 1999, ApJS, 123, 3
Massey, P., McNeill, R. T., Olsen, K. A. G., et al. 2007, AJ, 134, 2474
McCall, M. L. 2004, AJ, 128, 2144
McMillan, P. J. 2011, MNRAS, 414, 2446
McQuinn, K. B. W., Skillman, E. D., Dolphin, A. E., & Mitchell, N. P. 2015, ApJ, 808, 109
Melena, N. W., Elmegreen, B. G., Hunter, D. A., & Zernow, L. 2009, AJ, 138, 1203
Mel'Nik, A. M., & Efremov, Y. N. 1995, AstL, 21, 10
Melotte, P. J. 1926, MNRAS, 86, 636
Minniti, D., & Zijlstra, A. A. 1997, AJ, 114, 147
Postma, J., Hutchings, J. B., & Leahy, D. 2011, PASP, 123, 833
Postma, J. E., & Leahy, D. 2017, PASP, 129, 115002
Rejkuba, M., Minniti, D., Gregg, M. D., et al. 2000, AJ, 120, 801
Rubio, M., Elmegreen, B. G., Hunter, D. A., et al. 2015, Natur, 525, 218
Subramaniam, A., Sahu, S., Postma, J. E., et al. 2017, AJ, 154, 233
Sun, N.-C., de Grijs, R., Cioni, M.-R. L., et al. 2018, ApJ, 858, 31
Tandon, S. N., Subramaniam, A., Girish, V., et al. 2017, AJ, 154, 128
Thilker, D. A., Bianchi, L., Meurer, G., et al. 2007, ApJS, 173, 538
Tolstoy, E., Hill, V., & Tosi, M. 2009, ARA&A, 47, 371
Urbaneja, M. A., Kudritzki, R.-P., Bresolin, F., et al. 2008, ApJ, 684, 118
van der Marel, R. P., & Cioni, M.-R. L. 2001, AJ, 122, 1807
Weisz, D. R., Dalcanton, J. J., Williams, B. F., et al. 2011, ApJ, 739, 5
Whiting, A. B., Hau, G. K. T., & Irwin, M. 1999, AJ, 118, 2767
Zhang, H.-X., Hunter, D. A., Elmegreen, B. G., Gao, Y., & Schruba, A. 2012, AJ, 143, 47